RESEARCH ARTICLE

NANO · MICRO small
www.small-journal.com

Lead-Free, Sn-Based All-Perovskite Tandem Solar Cells with an Efficiency Over 15%

Saemon Yoon, Jun Ryu, SungWon Cho, Hyung Do Kim, Jongchul Lim, Jung Sang Cho,* Jongsung Park,* and Dong-Won Kang**

Recent advances in tin-based perovskite solar cells (TPSCs) have yielded significant gains in power conversion efficiency (PCE), yet progress on wide-bandgap (WBG) tin perovskites remains limited, primarily due to the complexities of halogen composition tuning and the associated phase segregation. Here, a halogen composition–independent strategy is presented for realizing WBG TPSCs by partially substituting formamidinium with dimethylammonium (DMA) in the A-site of the perovskite lattice. This substitution expands the lattice, widening the bandgap from 1.63 to 1.72 eV without requiring additional bromine. Comprehensive structural and optical analyses reveal enhanced crystallinity, reduced strain, and improved film morphology. Furthermore, ultraviolet photoelectron spectroscopy confirms enhanced band alignment with the hole transport layer, enabling more efficient charge extraction. By employing a dielectric/metal/dielectric transparent electrode, semi-transparent TPSCs (ST-TPSCs) are fabricated with a PCE of 10.37% and high near-infrared transmittance, which is well-suited for tandem applications. Stacking this ST-TPSC with a narrow-bandgap TPSC yields the first four-terminal, lead-free perovskite tandem device, achieving a combined PCE of 15.02%. These findings show that DMA incorporation effectively addresses the challenges of WBG TPSCs without relying on halogen adjustments, providing a robust pathway toward high-efficiency, eco-friendly photovoltaics and highlighting the promise of tin-based perovskites for next-generation tandem solar cells.

1. Introduction

The global pursuit of sustainable and eco-friendly energy solutions has accelerated the exploration of perovskite solar cells (PSCs) as promising candidates for next-generation photovoltaic technologies. Lead-based perovskites have demonstrated remarkable power conversion efficiencies (PCEs), exceeding 27% in single-junction devices and reaching up to 30.1% in tandem configurations, underscoring their potential to complement conventional silicon-based solar cells.[1,2] However, concerns regarding lead toxicity and its environmental impact have driven research into lead-free alternatives.[3,4] Among these, tin-based perovskite solar cells (TPSCs) hold particular promise due to the electronic similarity between tin and lead, offering a potential pathway to high-efficiency, lead-free PSCs.[5] Despite their potential, TPSCs have thus far lagged behind lead-based counterparts in both performance and stability, largely owing to the propensity of Sn^{2+} to oxidize to Sn^{4+}, creating deep-level

S. Yoon, J. Ryu, S. Cho
Department of Smart Cities
Chung-Ang University (CAU)
Seoul 06974, Republic of Korea

H. D. Kim
Department of Polymer Chemistry, Graduate School of Engineering
Kyoto University, Katsura Campus
Kyoto 615–8510, Japan

J. Lim
Graduate School of Energy Science and Technology
Chungnam National University
Daejeon 34134, Republic of Korea
E-mail: jclim@cnu.ac.kr

The ORCID identification number(s) for the author(s) of this article can be found under https://doi.org/10.1002/smll.202501876

DOI: 10.1002/smll.202501876

J. S. Cho
Department of Engineering Chemistry
Chungbuk National University
Chungbuk 28644, Republic of Korea
E-mail: jscho@chungbuk.ac.kr

J. S. Cho
Biomedical Research Institute
Chungbuk National University Hospital
Chungbuk 361-763 28644, Republic of Korea

J. S. Cho
Advanced Energy Research Institute
Chungbuk National University
Cheongju, Chungbuk 28644, Republic of Korea

J. Park
Department of Energy Engineering, Department of Energy System Engineering
Gyeongsang National University
Jinju, Gyeongnam 52828, Republic of Korea
E-mail: j.park@gnu.ac.kr

D.-W. Kang
Department of Energy Systems Engineering
Chung-Ang University (CAU)
Seoul 06974, Republic of Korea
E-mail: kangdwn@cau.ac.kr

Table 1. Lattice parameters, cell volumes, and bandgaps of tin-perovskites with and without DMA. (Lattice parameters and cell volumes were derived from Rietveld refinement of XRD data using the TOPAS, and Bandgaps were derived from Tauc plots).

Sample	$a = b$ [Å]	c [Å]	Volume [Å^3]	Bandgap [eV]
Control	8.8466(3)	12.5478(4)	982.03	1.63
Target	8.8988(2)	12.5394(4)	992.97	1.72

traps that hinder charge transport and increase recombination losses.[6,7] To address these challenges and advance TPSCs toward practical applications, recent efforts have focused on enhancing both performance and stability, including the strategic use of additives and compositional engineering. For instance, incorporating certain additives has led to PCEs of up to 15.38% for narrow-bandgap (NBG) TPSCs (1.36 eV) and 12.22% for wide-bandgap (WBG) devices (1.65 eV) in our group's previous work.[8,9] However, lead-free perovskite tandem solar cells remain relatively underexplored. In many cases, studies on WBG TPSCs suitable for tandem top cells have been largely confined to simulations, illustrating the inherent difficulties in translating these concepts into high-performance, experimentally demonstrated devices.[10–15]

To create WBG tin-based perovskites, most strategies focus on adjusting the halide ratio by reducing iodide content while increasing bromide content. Unfortunately, such compositional changes frequently induce phase segregation and modify microstructural properties, including crystal lattice stability, nucleation kinetics, and defect density, complicating crystal growth control and undermining film quality. An alternative route to improving WBG TPSCs is to engineer the perovskite's A-site by incorporating larger organic cations. Dimethylammonium (DMA) is one such candidate that can modify both the structural and electronic characteristics of perovskites. In lead-based systems, DMA incorporation has been shown to enhance crystallinity, passivate defects, and widen the bandgap via lattice parameter modulation.[16–20] These observations suggest that DMA may also effectively address persistent challenges in WBG TPSCs. Yet, comprehensive investigations into how DMA influences the crystal structure, energy levels, and morphology in WBG TPSCs are still limited, leaving a significant knowledge gap in this domain.

Recognizing that WBG tin perovskites must combine both high efficiency and adequate transparency to function as top cells in lead-free tandem architectures, we systematically explore the incorporation of DMA into tin-based perovskites to produce photoactive materials suitable for tandem applications. By partially substituting formamidinium (FA) with DMA in the perovskite's A-site, we aim to achieve lattice expansion, bandgap widening, and more favorable energy-level alignment with the hole transport layer (HTL). X-ray diffraction (XRD) and Rietveld refinement reveal that DMA incorporation increases the lattice parameters a and b, slightly reduces c, and expands the overall unit cell volume. As a result, the bandgap widens from 1.63 to 1.72 eV due to decreased orbital overlap between the metal cation and halide ions. Furthermore, the presence of DMA improves crystallinity, reduces strain and dislocation density, and leads to a more uniform film morphology. Ultraviolet photoelectron spectroscopy (UPS) confirms that DMA incorporation shifts the perovskite's energy levels to better align with PEDOT:PSS (the HTL), tuning the energy barrier for hole transport from −0.17 eV in the control sample to +0.16 eV in the DMA-modified device. This enhanced alignment facilitates efficient charge extraction and reduces recombination losses.

We then integrate a dielectric/metal/dielectric (DMD) structured electrode composed of Sb_2O_3/Ag/Sb_2O_3 to fabricate semi-transparent TPSCs (ST-TPSCs). These devices exhibit both high visible-light transmittance and robust photovoltaic performance, with negligible loss in transparency compared to the bare perovskite film. Our DMA-modified ST-TPSC achieves a PCE of 10.37%, which is about a 44% improvement over the 7.21% PCE of the control device, while maintaining near-infrared (NIR) transmittance of ≈60%. Such optical and electrical properties make the device highly suitable as a top cell in tandem configurations.

Finally, to showcase the practical utility of our DMA-incorporated WBG perovskite, we stack the ST-TPSC atop an NBG (1.41 eV) TPSC, creating a four-terminal (4T), lead-free tandem solar cell. The NBG TPSC achieves a PCE of 11.61%, and when illuminated through the top ST-TPSC, it delivers 4.66%. Overall, the 4T tandem device reaches a combined PCE of 15.02%, surpassing the performance of most single-junction TPSCs and emphasizing the promise of tandem architectures in overcoming the intrinsic bandgap limitations of individual perovskite devices.

2. Results and Discussion

To optimize current matching for the top cell in a tandem device employing an NBG TPSC (≈1.4 eV), we initially investigated how halide composition tuning affects the $ASnI_2Br$ perovskite (bandgap = 1.63 eV). Our goal was to fabricate a perovskite with an expanded bandgap by modifying the SnX_6 octahedra with smaller halide ions. By decreasing the iodine fraction and increasing the proportion of bromine—which has a smaller ionic radius—we successfully widened the bandgap to 1.83 eV (Figure S1, Supporting Information). However, photoluminescence (PL) measurements revealed severe difficulties in morphology control and stable perovskite phase formation, resulting in extremely low radiative recombination and a PCE below 1%. We also explored a composition incorporating chlorine, previously reported to facilitate stable phase formation while simultaneously suppressing phase separation,[21] which achieved a 1.72 eV bandgap. Still, it did not yield material properties suitable for tandem top-cell applications. Consequently, we opted for an alternative strategy to increase the bandgap, hypothesizing that the incorporation of a larger organic cation into the A-site—rather than solely adjusting the halide ratio—could reshape the SnX_6 octahedra and thereby tune the bandgap. Based on this rationale, we chose DMA, an organic cation large enough to avoid favoring the formation of 2D phases.

To examine the effect of DMA on crystal formation in $ASnI_2Br$ perovskites, we performed XRD measurements (Figure S2, Supporting Information) followed by Rietveld refinement to elucidate structural changes. In this study, the control sample is defined as $(FA_{0.8}PEA_{0.1}EA_{0.1})_{0.98}EDA_{0.01}SnI_2Br$ (no DMA), while the target sample is $(FA_{0.7}PEA_{0.1}EA_{0.1}DMA_{0.1})_{0.98}EDA_{0.01}SnI_2Br$, where FA is partially replaced by DMA at the A-site (see

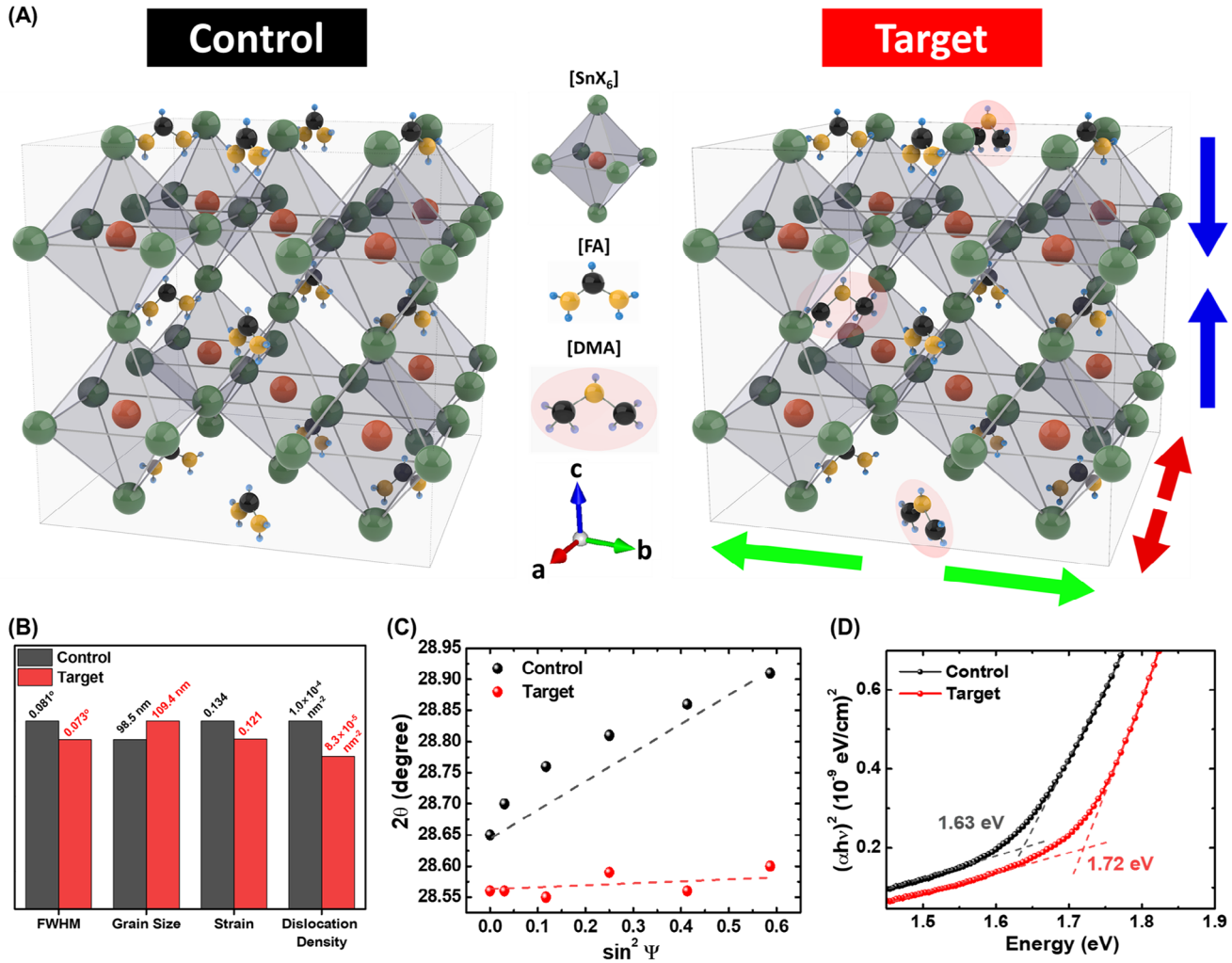

Figure 1. Structural and electronic analyses of control and target samples. A) Crystal structures illustrating lattice deformation, B) crystallographic parameters obtained from XRD analysis, C) strain distribution at the (220) plane for the compressive-strained film, with measured data and fitted lines plotted against $\sin^2\psi$, and D) Tauc plots indicating the bandgap of the samples.

Supporting Information for detailed preparation methods). Comparing the XRD patterns, the main peaks for the (110) and (220) planes in the control perovskite at 14.23° and 28.64° shift to 14.19° and 28.55° in the target sample, indicating lattice expansion driven by DMA incorporation. The lattice parameters and cell volumes, refined within the tetragonal P4bm space group, are summarized in **Table 1**.

Substituting DMA, a larger organic cation, for FA increases the ***a*** and ***b*** lattice parameters while slightly reducing ***c***, resulting in an overall volume expansion of ≈11 Å^3, This structural modification confers several advantages. The expansion of ***a*** and ***b*** diminishes orbital overlap between the metal and halide ions, thus broadening the bandgap. Meanwhile, the slight contraction along ***c*** may enhance structural stability and potentially alleviate anisotropic strain in the lattice.[5] **Figure 1A** provides an illustration of this lattice distortion. To further investigate the crystallographic implications of DMA incorporation, we extracted the full width at half maximum (FWHM), average crystallite size, strain, and dislocation density using the Debye-Scherrer and Williamson–Hall method (see Supporting Information for details).

As presented in Figure 1B, the grain size of the target sample increases from 98.5 to 109.4 nm compared to the control, while the FWHM, strain, and dislocation density all decrease. The FWHM corresponds to the (110) plane, suggesting enhanced crystallinity in the film.[22] To investigate the lattice strain in more detail, Grazing Incidence X-ray Diffraction (GIXRD) measurements (Figure S3, Supporting Information) were conducted, and the strain distribution was analyzed via the 2θ versus $\sin^2\psi$ method, where ψ represents the tilt angle. As shown in Figure 1C, the strain distribution at the (220) plane is plotted against $\sin^2\psi$ for both the control and target samples. The control sample experiences compressive strain, likely induced by compositional non-uniformity within the perovskite film, which can detrimentally affect charge-carrier dynamics and elevate defect density, thereby promoting recombination.[23] In contrast, the target sample—incorporating DMA—exhibits reduced compressive strain, attributable to lattice expansion facilitated by the

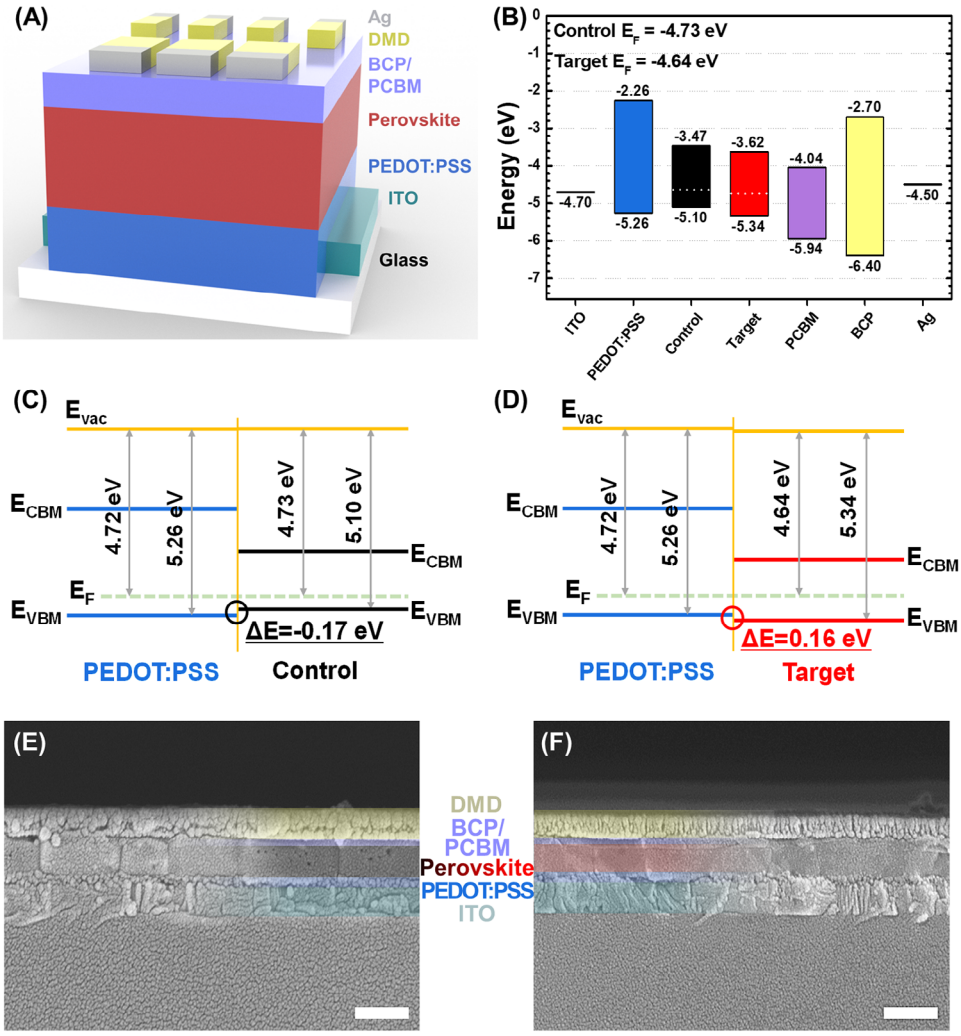

Figure 2. A) Schematic of the ST-TPSC device structure and B) corresponding energy-level diagram. C,D) Energy band alignment for the control and target devices, respectively, and E,F) cross-sectional FE-SEM images for each device (scale bar = 300 nm). The perovskite layers are highlighted in both FE-SEM images.

larger ionic radius of DMA (272 pm) relative to FA (253 pm).[24] This expansion offsets inherent compressive forces in the crystal structure, effectively minimizing overall strain. Moreover, improved crystallinity and a more uniform film morphology help distribute stress more evenly across the entire film, further mitigating strain.[25] Notably, our crystallographic analysis of DMA in tin-based perovskites diverges from previous studies. In lead-based perovskites, for example, DMA incorporation for WBG development has been primarily attributed to octahedral tilting,[26] whereas another investigation examined DMA in tin-based single-halide perovskites for defect and trap-density suppression, without delving into detailed crystallographic effects.[27] In contrast, this work precisely quantifies lattice parameter shifts and provides an in-depth Rietveld refinement to elucidate the crystallographic impact of DMA in tin-based WBG mixed-halide perovskites.

Figure 1D displays Tauc plots derived from optical absorption measurements for the control and target films, indicating bandgaps of 1.63 and 1.72 eV, respectively. To further validate these bandgap modifications, PL spectra were measured (Figure S4, Supporting Information). The PL peaks correspond to the bandgap values, corroborating the observed bandgap widening. Both Tauc plots and PL spectra follow the same trend, confirming that DMA incorporation effectively expands the bandgap. Overall, the enhancements in lattice parameters and crystallinity introduced by DMA not only broaden the bandgap and improve the absorption profile, but also alleviate strain, collectively promising improved device performance.

To demonstrate the suitability of our ST-TPSCs as top cells in lead-free tandem PSCs, we employed a DMD-structured transparent electrode consisting of Sb_2O_3/Ag/Sb_2O_3.[28] The device structure is depicted in **Figure** 2A, while Figure 2B illustrates the energy-level diagram. The energy levels of PEDOT:PSS and the perovskite films were determined from UPS measurements (Figure S5, Supporting Information) and the bandgaps shown in Figure 1D. These UPS spectra and bandgap data provide the conduction band minimum (CBM), Fermi level (E_F), and valence band maximum (VBM) for each material. When the perovskite

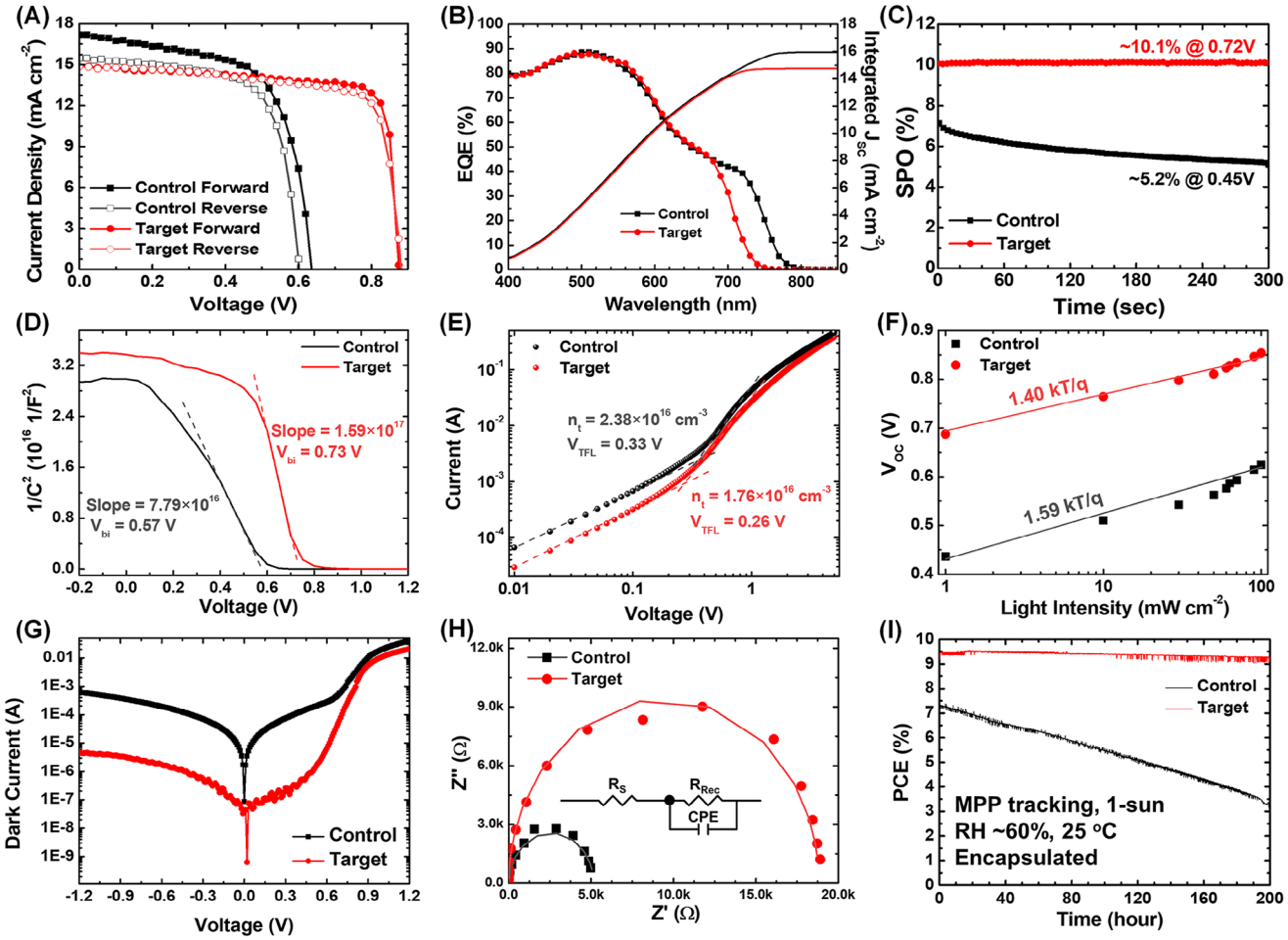

Figure 3. A) *J–V* characteristics obtained from forward and reverse scans, B) EQE spectra, C) steady-state power output (SPO) measurements, D) Mott–Schottky analyses, E) SCLC measurements, F) LIDV results, G) dark current measurements, H) Nyquist plots for resistance analyses, and I) long-term operational stability of the control and target devices.

and PEDOT:PSS layers form a junction, their Fermi levels align to establish equilibrium, causing shifts in both the vacuum level (E_{vac}) and the energy levels of the perovskite. In our calculations, E_{vac} in the control sample shifts upward by 0.01 eV, whereas in the target sample, it shifts downward by 0.08 eV. This energy band alignment is depicted for both the control and target devices in Figure 2C,D, respectively. The energy offset indicates that the tin perovskite in the control device faces a 0.17 eV barrier for hole transport to the PEDOT:PSS layer, thereby impeding efficient extraction and adversely affecting device performance. Conversely, the VBM of the tin perovskite in the target device is 0.16 eV below that of PEDOT:PSS, favoring hole transport from the absorber to PEDOT:PSS. This enhanced alignment boosts charge extraction, diminishes recombination losses, and consequently improves device performance. By incorporating DMA, we effectively shift the perovskite's energy levels, optimizing alignment with PEDOT:PSS and reducing the hole-transport barrier from +0.17 eV in the control device to −0.16 eV in the target device (Figure 2C,D). Such favorable band alignment can significantly raise the open-circuit voltage (V_{OC}) and overall device efficiency.

Figure 2E,F show cross-sectional field-emission scanning electron microscopy (FE-SEM) images of the control and target devices, respectively, with the perovskite layers highlighted for clarity. In the control device, voids and pinholes attributed to defects are visible within the perovskite film, potentially serving as recombination centers that degrade performance. These defects are also confirmed by surface imagery in Figure S6A (Supporting Information). In contrast, the target perovskite layer is more uniform and densely packed, exhibiting fewer defects, as evidenced in Figure S6B (Supporting Information). The reduction in compressive strain achieved via DMA incorporation not only strengthens crystallinity but also refines film morphology. Such morphological improvements are crucial for enhancing device performance, as they promote efficient charge transport and curb recombination.[29] A uniform, defect-free perovskite layer establishes superior interfaces with adjacent layers, enabling more effective charge extraction and collection.

The transmittance spectra of the perovskite films and the fabricated ST-TPSCs, along with actual device images, are shown in Figure S7 (Supporting Information). Notably, the visible-light transmittance of the ST-TPSC device closely matches that of the

Table 2. Photovoltaic performance summary of the champion devices and averages.

–	–	V_{OC} [V]	J_{SC} [mA cm^{-2}]	FF	PCE [%]
Control Champion	Forward	0.64	17.18	0.659	7.21
	Reverse	0.60	15.46	0.683	6.35
Control Average		0.59 (±0.03)	16.42 (±0.61)	0.667 (±0.02)	6.47 (±0.63)
Target Champion	Forward	0.88	14.88	0.796	10.37
	Reverse	0.88	14.87	0.753	9.88
Target Average		0.84 (±0.03)	14.39 (±0.31)	0.744 (±0.02)	9.00 (±0.59)

bare perovskite film, indicating that the DMD electrode imposes minimal interference. Consequently, the integration of the DMD electrode preserves high transparency in the visible range. Although the DMD electrode exhibits some limitations in the NIR region above ≈750 nm, the ST-TPSCs achieve an NIR transmittance of ≈60%, which is sufficient for use as the top cell in tandem solar configurations. **Figure** 3A presents the *J*–*V* characteristics of the ST-TPSCs, and **Table** 2 summarizes the champion and average device parameters for both control and target samples. Box plots in Figure S8 (Supporting Information) further confirm the reliability of these parameters.

Transitioning from the control to the target device—with its wider bandgap—enhances the V_{OC} while reducing the short-circuit current density (J_{SC}). Specifically, the V_{OC} increases by ≈38% (from 0.64 to 0.88 V), whereas the J_{SC} decreases by roughly 13% (from 17.18 to 14.88 mA cm^{-2}). This favorable trade-off arises from DMA's role in both widening the bandgap and improving the crystallinity and energy band alignment of the perovskite layer. Reflecting these improvements, the fill factor (FF) rises from 0.659 to 0.796, resulting in an overall PCE of 10.37%, which represents a substantial 44% increase over the control's 7.21%. Nevertheless, despite these promising enhancements, the observed V_{OC} (≈0.84 V) remains below expectations given the relatively wide bandgap of 1.72 eV. Such a discrepancy primarily originates from intrinsic limitations specific to Sn-based perovskites. The highly reactive Sn^{2+} ions readily oxidize to Sn^{4+}, substantially increasing defect densities, thereby creating abundant non-radiative recombination centers. Additionally, suboptimal interfacial energy alignment further exacerbates these recombination losses, collectively limiting the achievable V_{OC}, as extensively documented in prior studies.[9] To overcome these inherent constraints, we investigated alternative electron transport layers (ETLs), notably indene-C60 bisadduct (ICBA), which is known for its lower interfacial energy losses compared to the commonly used PCBM. Indeed, our preliminary results demonstrated that ICBA notably improved V_{OC} from 0.86 to ≈1.00 V (Figure S9, Supporting Information). Unfortunately, practical processing challenges, including limited solubility and severe aggregation of ICBA films, significantly compromised both FF and J_{SC}, ultimately reducing the overall PCE. These findings emphasize the necessity of further systematic optimization of ETL processing and interfacial engineering to fully leverage the benefits of alternative ETLs. External quantum efficiency (EQE) spectra in Figure 3B confirm that the bandgap widening narrows the spectral absorption range. The integrated J_{SC} values from EQE measurements are 15.96 mA cm^{-2} for the control and 14.75 mA cm^{-2} for the target, consistent with the average J_{SC} obtained from the *J*–*V* characteristics (16.42 vs 14.39 mA cm^{-2}, respectively). The negligible deviation between EQE and *J*–*V* results validate both the device quality and the measurement accuracy. In the control device, the reverse-scan J_{SC} (15.46 mA cm^{-2}) is 1.72 mA cm^{-2} lower than that measured in the forward scan (17.18 mA cm^{-2}), revealing a discrepancy of roughly 10%. This instability is also evident in the steady-state power output (SPO) measurements (Figure 3C), where the control's PCE declines during a 5-min test under V_{MPP} bias. This difference under illumination was further confirmed through PL measurements performed on WBG perovskite films under continuous 1-sun illumination over a defined period (Figure S10, Supporting Information). The results clearly demonstrate that halide phase segregation in the control film rapidly intensified with illumination time, whereas it was significantly delayed in the target film. These issues likely stem from defects, suboptimal energy band alignment, and phase degradation leading to hysteresis and reduced device reliability.

Various electrochemical analyses were conducted to gain deeper insight into the device performance. In the Mott–Schottky analysis derived from capacitance–voltage measurements (Figure 3D), the slope is inversely proportional to the charge-carrier density. The target device exhibits a steeper slope than the control, indicating a higher charge-carrier density that significantly enhances photocurrent and overall device efficiency.[30] This improvement in charge-carrier density promotes more efficient charge transport and reduces resistive losses. The built-in potentials (V_{bi}) for the target and control devices were measured to be 0.73 and 0.57 V, respectively, with the higher V_{bi} in the target device facilitating carrier separation and transport—consistent with the observed increase in V_{OC}.[31,32]

To quantify the trap density of states (N_t), hole-only devices (ITO/PEDOT:PSS/perovskite/P3HT/Au) were prepared. From the space charge limited current (SCLC) measurements, the trap-filled limit voltage (V_{TFL}) values for the control and target devices were 0.33 and 0.26 V, respectively (Figure 3E). Accordingly, the N_t of the target device decreased from 2.38×10^{16} to 1.76×10^{16} cm^{-3}, illustrating how DMA incorporation improves crystallinity and reduces defect formation. Figure 3F depicts the light-intensity-dependent V_{OC} (LIDV) for both the control and target devices. The slope relative to kT/q indicates the degree of trap-assisted recombination, the target's slope is 1.40 kT q^{-1}, while the control's is 1.59 kT q^{-1}. This closer-to-unity slope in the target device signifies lower trap-assisted recombination compared to the control.

Dark current measurements under zero illumination (Figure 3G) reveal a reduced dark current in the target device, attributed to the improved film morphology and diminished trap

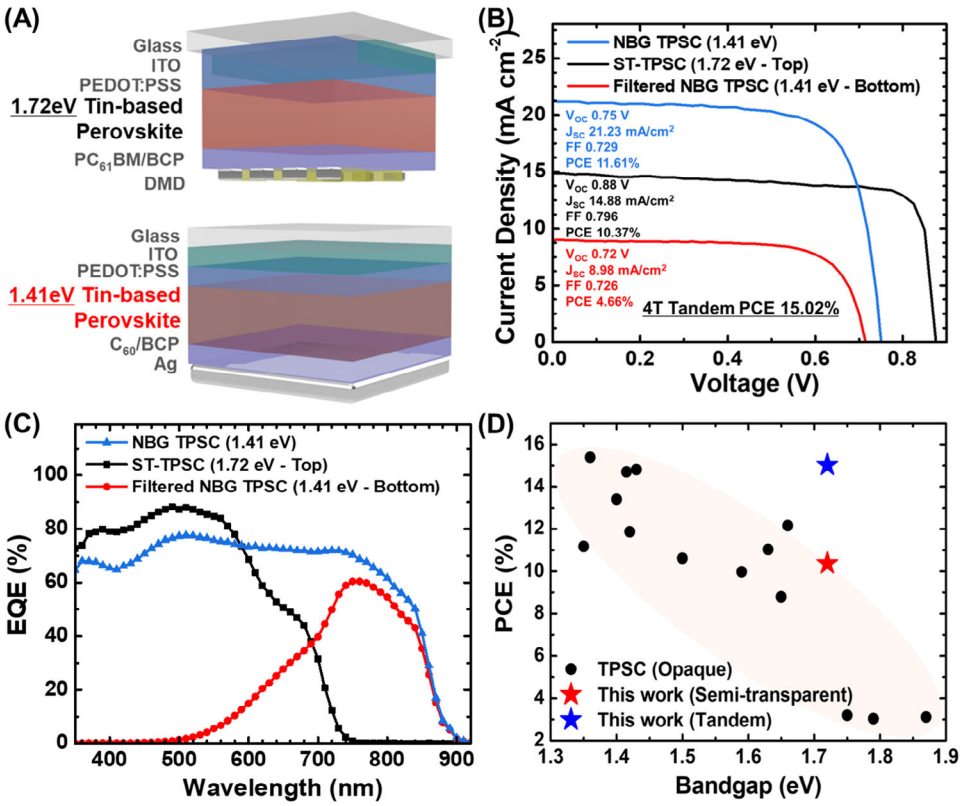

Figure 4. A) Schematic illustration of the device configuration, B) *J–V* curves and corresponding performance parameters, C) EQE spectra of the ST-TPSC and the 4T lead-free perovskite tandem solar cell, D) A comparative plot of PCE versus bandgap, highlighting the performance of the present work relative to previously reported TPSCs.

density facilitated by DMA incorporation. This reduction in dark current indicates fewer non-radiative recombination centers and defect states, thus enhancing device efficiency.[33] Nyquist plots obtained from impedance spectroscopy (Figure 3H) confirm these findings, the target device exhibits a recombination resistance (R_{Rec}) nearly four times higher than that of the control, underscoring its superior capability to suppress recombination. Detailed fitted values are summarized in Table S1 (Supporting Information), and the high-frequency region of the Nyquist plot (series resistance, R_s) is shown in Figure S11 (Supporting Information). Consistent with the higher charge-carrier density revealed by Mott–Schottky analysis, the target device's R_s is approximately half that of the control. Under continuous operation at the maximum power point for 200 h in an air environment at >60% relative humidity—and with encapsulation—the target device retains over 97% of its initial PCE, whereas the control maintains only ≈45% (Figure 3I). These results highlight the significantly enhanced stability of ST-TPSCs upon DMA incorporation, which not only bolsters crystallographic stability but also benefits overall device performance. Building on these findings, we fabricated monolithic lead-free perovskite tandem solar cells employing a DMA-incorporated WBG tin-based perovskite (bandgap: 1.72 eV) and an NBG tin-based perovskite (bandgap: 1.41 eV). The tandem cell configuration is ITO/PEDOT:PSS/WBG tin-based perovskite/PCBM/BCP/Ag/MoO_3/PEDOT:PSS/NBG tin-based perovskite/PCBM/BCP/Ag. A representative cross-sectional FE-SEM image of the tandem cells is provided in Figure S12A (Supporting Information). Figure S12B (Supporting Information) shows the *J–V* curve of the best-performing monolithic tandem cell, achieving a PCE of 4.14%, V_{OC} of 1.06 V, J_{SC} of 6.88 mA cm^{-2}, and FF of 0.568. However, the interconnection layer (ICL) composed of Ag/MoO_3 proved insufficient in shielding against solvent damage from the spin-coating of PEDOT:PSS and the NBG tin-based perovskite, resulting in low yields and limited tandem-device performance. Employing conventional sputtered indium tin oxide (ITO) as the ICL introduces an additional challenge: mitigating plasma damage to the underlying perovskite layers during sputtering.[34] Alternative methods, such as atomic layer deposition (ALD) of SnO_x, were also considered, however, the use of water as a precursor in ALD presents challenges for tin-based perovskites, which are prone to moisture-induced degradation.[35] Consequently, such approaches may not be optimal for our devices. Future efforts will focus on developing a new ICL capable of affording effective protection during subsequent solution processes, without damaging underlying perovskite layers. This ICL must exhibit robust electrical conductivity, optical transparency, and chemical stability to enable high-performance, monolithic lead-free perovskite tandem solar cells.

To explore a more advanced application of our ST-TPSC, we assembled a 4T tandem device by vertically stacking a single-junction ST-TPSC and an NBG TPSC. The schematic depiction

of this 4T tandem configuration appears in **Figure** 4A. As shown in Figure 4B, the NBG TPSC alone delivers a PCE of 11.61% (V_{OC} = 0.75 V, J_{SC} = 21.23 mA cm^{-2}, FF = 0.729). In designing this NBG TPSC, we carefully considered the impact of incorporating DMA. Although DMA effectively stabilizes Sn^{2+} ions and reduces defect density, it inherently increases the perovskite bandgap from 1.41 to ≈1.5 eV. This shift would significantly decrease NIR absorption, thereby negatively affecting J_{SC} and complicating current matching between the top and bottom cells. To avoid these limitations, DMA was intentionally omitted from the NBG layer, ensuring optimal compatibility with our tandem structure. When the same device operates under illumination filtered by the overlying ST-TPSC, its PCE remains at 4.66% (V_{OC} = 0.72 V, J_{SC} = 8.98 mA cm^{-2}, FF = 0.726). Consequently, the combined PCE for the tandem device, encompassing the top ST-TPSC and the bottom filtered NBG TPSC, reaches 15.02%. This result underscores the effectiveness of the 4T architecture in harnessing a broader spectral range. We further optimized the thickness of the NBG perovskite films to maximize tandem performance. In Figure S13 (Supporting Information), thinner films (fabricated at 5000 rpm) achieved standalone PCE exceeding 13%, approaching values reported in recent high-performance literature. However, under tandem-filtered illumination conditions, these thinner films exhibited a pronounced reduction in EQE within the NIR region, resulting in a substantial decline in J_{SC} and overall PCE (≈4.3%). In contrast, slightly thicker films (fabricated at 3000 rpm), despite exhibiting lower standalone efficiencies (11.61%), retained relatively higher efficiencies (4.66%) under tandem-filtered conditions, demonstrating superior suitability for integration in the tandem device. We acknowledge that further enhancements in NBG cell PCE beyond 14% would require considerable improvements in V_{OC}. Achieving such enhancements would necessitate significant modifications to the ETL (e.g., replacing C60 with ICBA) and additional optimization strategies including perovskite surface treatments and additives. Due to practical constraints within the current scope, these optimizations remain challenging but represent important directions for future investigation. The EQE spectra, displayed in Figure 4C, further validate that the bottom NBG device efficiently absorbs photons transmitted by the top ST-TPSC. Specifically, the ST-TPSC exhibits robust EQE in the spectral region corresponding to its widened bandgap, while the NBG device displays an extended EQE profile at longer wavelengths, capturing the transmitted photons. Notably, the PCE–bandgap plot in Figure 4D highlights two key achievements of this work: i) the highest PCE reported to date for WBG (>1.7 eV) ST-TPSCs, and ii) superior performance in fully lead-free, all-perovskite tandem cells. As summarized in Table S2 (Supporting Information), our 4T tandem PCE of 15.02% surpasses the efficiencies of most single-junction T PSCs, illustrating how tandem architecture can effectively overcome the bandgap limitations of individual devices.

3. Conclusion

In summary, DMA incorporation into tin-based perovskites substantially elevates both their structural and electronic characteristics, rendering them highly suitable for WBG applications in tandem photovoltaics. Substituting a fraction of the FA cations with DMA at the A-site induces lattice expansion, broadens the bandgap from 1.63 to 1.72 eV, and optimizes energy-level alignment with the hole transport layer. These effects collectively improve crystallinity, minimize lattice strain, and enhance film morphology. As a result, our fabricated ST-TPSC achieves a notable PCE of 10.37% while preserving strong near-infrared transmittance. Furthermore, by integrating the ST-TPSC as the top cell and the NBG TPSC as the bottom cell in a four-terminal tandem configuration, we attain a combined PCE of 15.02%, the highest reported to date in fully lead-free perovskite tandem systems. This work thereby outlines a promising route for advancing eco-friendly solar cell technologies, emphasizing the pivotal role of tandem device architectures in alleviating bandgap constraints to achieve high efficiencies.

4. Experimental Section

Experimental procedures can be found in the Supporting Information.

Supporting Information

Supporting Information is available from the Wiley Online Library or from the author.

Acknowledgements

The present research was supported by the National Research Foundation of Korea (NRF) funded by the Korea government (MSIT) (NRF- RS-2023-00217270, RS-2023-00212744, 2023K2A9A2A08000151 and RS-2024-00436187).

Conflict of Interest

The authors declare no conflict of interest.

Data Availability Statement

The data that support the findings of this study are available in the supplementary material of this article.

Keywords

dimethylammonium incorporation, lead-free tandem solar cells, semi-transparent, tin-based perovskites, wide bandgap

Received: February 13, 2025
Revised: March 13, 2025
Published online:

[1] National Renewable Energy Laboratory, *Best Research Cell Efficiency Chart*, National Renewable Energy Laboratory, Golden, Colorado **2025**.
[2] M. A. Green, E. D. Dunlop, M. Yoshita, N. Kopidakis, K. Bothe, G. Siefer, X. Hao, J. Y. Jiang, *Prog. Photovoltaics* **2025**, *33*, 3.

[3] M. Wang, W. Wang, B. Ma, W. Shen, L. Liu, K. Cao, S. Chen, W. Huang, *Nanomicro Lett.* **2021**, *13*, 62.
[4] T. Wu, X. Liu, X. Luo, X. Lin, D. Cui, Y. Wang, H. Segawa, Y. Zhang, L. Han, *Joule* **2021**, *5*, 863.
[5] C. Grote, R. F. Berger, *J. Phys. Chem. C* **2015**, *119*, 22832.
[6] T. Leijtens, R. Prasanna, A. Gold-Parker, M. F. Toney, M. D. McGehee, *ACS Energy Lett.* **2017**, *2*, 2159.
[7] T. B. Song, T. Yokoyama, C. C. Stoumpos, J. Logsdon, D. H. Cao, M. R. Wasielewski, S. Aramaki, M. G. Kanatzidis, *J. Am. Chem. Soc.* **2017**, *139*, 836.
[8] T. Li, F. He, J. Liang, Y. Qi, *Joule* **2023**, *7*, 1966.
[9] P. Pandey, S. Cho, J. Bahadur, S. Yoon, C. M. Oh, I. W. Hwang, H. Song, H. Choi, S. Hayase, J. S. Cho, D. W. Kang, *Adv. Energy Mater.* **2024**, *14*, 2401188.
[10] J. Madan, Shivani, R. Pandey, R. Sharma, *Sol. Energy* **2020**, *197*, 212.
[11] N. Singh, A. Agarwal, M. Agarwal, *Sol. Energy* **2020**, *208*, 399.
[12] R. Pandey, S. Sharma, J. Madan, R. Sharma, *J. Micromech. Microeng.* **2021**, *32*, 014004.
[13] N. Singh, A. Agarwal, M. Agarwal, *Superlattices Microstruct.* **2021**, *149*, 106750.
[14] S. Abdelaziz, A. Zekry, A. Shaker, M. Abouelatta, *Opt. Mater.* **2022**, *123*, 111893.
[15] A. U. Duha, M. F. Borunda, *Opt. Mater.* **2022**, *123*, 111891.
[16] H. Chen, Q. Wei, M. I. Saidaminov, F. Wang, A. Johnston, Y. Hou, Z. Peng, K. Xu, W. Zhou, Z. Liu, L. Qiao, X. Wang, S. Xu, J. Li, R. Long, Y. Ke, E. H. Sargent, Z. Ning, *Adv. Mater.* **2019**, *31*, 1903559.
[17] G. E. Eperon, K. H. Stone, L. E. Mundt, T. H. Schloemer, S. N. Habisreutinger, S. P. Dunfield, L. T. Schelhas, J. J. Berry, D. T. Moore, *ACS Energy Lett.* **2020**, *5*, 1856.
[18] S. Jariwala, R. E. Kumar, G. E. Eperon, Y. Shi, D. P. Fenning, D. S. Ginger, *ACS Energy Lett.* **2021**, *7*, 204.
[19] J. Zhao, H. Wang, L. Duan, T. Lv, B. Xiao, J. Zhang, J. Liu, Y. Zhang, Q. Liu, *Sol. RRL* **2021**, *6*, 2100923.
[20] H. Cheng, Y. Feng, Y. Fu, Y. Zheng, Y. Shao, Y. Bai, *J. Mater. Chem. C* **2022**, *10*, 13590.
[21] J. Cho, P. V. Kamat, *Chem. Mater.* **2020**, *32*, 6206.
[22] J. Bahadur, S. Cho, P. Pandey, S. Yoon, D. G. Lee, J. Ryu, J. T. Song, J. Lim, D. W. Kang, *Sol. RRL* **2024**, *8*, 2300912.
[23] M. Hu, R. Nie, H. Kim, J. Wu, S. Chen, B.-w. Park, G. Kim, H.-W. Kwon, S. I. Seok, *ACS Energy Lett.* **2021**, *6*, 3555.
[24] G. Kieslich, S. Sun, A. K. Cheetham, *Chem. Sci.* **2014**, *5*, 4712.
[25] B. Yang, D. Bogachuk, J. Suo, L. Wagner, H. Kim, J. Lim, A. Hinsch, G. Boschloo, M. K. Nazeeruddin, A. Hagfeldt, *Chem. Soc. Rev.* **2022**, *51*, 7509.
[26] R. Prasanna, A. Gold-Parker, T. Leijtens, B. Conings, A. Babayigit, H. G. Boyen, M. F. Toney, M. D. McGehee, *J. Am. Chem. Soc.* **2017**, *139*, 11117.
[27] M. A. Kamarudin, S. R. Sahamir, K. Nishimura, S. Iikubo, K. Yoshino, T. Minemoto, Q. Shen, S. Hayase, *ACS Mater. Lett.* **2022**, *4*, 1855.
[28] S. Song, H. W. Cho, J. Jeong, Y. J. Yoon, S. Y. Park, S. Song, B. H. Woo, Y. C. Jun, B. Walker, J. Y. Kim, *Sol. RRL* **2020**, *4*, 2000201.
[29] S. Sanchez, L. Pfeifer, N. Vlachopoulos, A. Hagfeldt, *Chem. Soc. Rev.* **2021**, *50*, 7108.
[30] O. Almora, C. Aranda, E. Mas-Marzá, G. Garcia-Belmonte, *Appl. Phys. Lett.* **2016**, *109*, 173903.
[31] A. Guerrero, E. J. Juarez-Perez, J. Bisquert, I. Mora-Sero, G. Garcia-Belmonte, *Appl. Phys. Lett.* **2014**, *105*, 133902.
[32] S. M. Sze, Y. Li, K. K. Ng, *Physics of Semiconductor Devices*, John Wiley & Sons, Hoboken, New Jersey, **2021**.
[33] W. Ke, C. C. Stoumpos, I. Spanopoulos, M. Chen, M. R. Wasielewski, M. G. Kanatzidis, *ACS Energy Lett.* **2018**, *3*, 1470.
[34] S.-H. Lim, H.-J. Seok, M.-J. Kwak, D.-H. Choi, S.-K. Kim, D.-H. Kim, H.-K. Kim, *Nano Energy* **2021**, *82*, 105703.
[35] A. Hultqvist, T. J. Jacobsson, S. Svanström, M. Edoff, U. B. Cappel, H. Rensmo, E. M. Johansson, G. Boschloo, T. Törndahl, *ACS Appl. Energy Mater.* **2021**, *4*, 510.